

Three oxime ether derivatives: Synthesis, crystallographic study, electronic structure and molecular electrostatic potential calculation



Tanusri Dey^a, Koduru Sri Shanthi Praveena^b, Sarbani Pal^b, Alok Kumar Mukherjee^{a,*}

^a Department of Physics, Jadavpur University, Kolkata 700032, India

^b Department of Chemistry, MNR Degree and PG College, Kukatpally, Hyderabad 500085, India

ARTICLE INFO

Article history:

Received 18 October 2016

Received in revised form

17 January 2017

Accepted 23 February 2017

Available online 24 February 2017

Keywords:

Oxime ether derivative

X-ray powder diffraction

Hirshfeld surface analysis

Molecular electrostatic potential

Electronic structure

ABSTRACT

Three oxime ether derivatives, (*E*)-3-methoxy-4-(prop-2-ynyloxy)-benzaldehyde-*O*-prop-2-ynyl-oxime (C₁₄H₁₃NO₃) (**2**), benzophenone-*O*-prop-2-ynyl-oxime (C₁₆H₁₃NO) (**3**) and (*E*)-2-chloro-6-methylquinoline-3-carbaldehyde-*O*-prop-2-ynyl-oxime (C₁₄H₁₁ClN₂O) (**4**), have been synthesized and their crystal structures have been determined. The DFT optimized molecular geometries in **2–4** agree closely with those obtained from the crystallographic study. An interplay of intermolecular C–H···O, C–H···N, C–H···Cl and C–H···π(arene) hydrogen bonds and π···π interactions assembles molecules into a 2D columnar architecture in **2**, a 1D molecular ribbon in **3** and a 3D framework in **4**. Hirshfeld surface analysis showed that the structures of **2** and **3** are mainly characterized by H···H, H···C and H···O contacts but some contribution of H···N and H···Cl contacts is also observed in **4**. Hydrogen-bond based interactions in **2–4** have been complemented by calculating molecular electrostatic potential (MEP) surfaces. The electronic structures of molecules reveal that the estimated band gap in **3**, in which both aldehyde hydrogen atoms of formaldehyde-*O*-prop-2-ynyl-oxime (**1**) have been substituted by two benzene rings, is higher than that of **2** and **4** with only one aldehyde hydrogen atom replaced.

© 2017 Elsevier B.V. All rights reserved.

1. Introduction

Intermolecular interactions, in particular, hydrogen bonds, have been a topic of considerable importance due to their role in crystal engineering and biological recognition process [1–3]. Many of the synthons identified in supramolecular chemistry involve N/O–H···O/N hydrogen bonds, which provide the required selectivity and directionality to control molecular aggregation [4,5]. In addition to these relatively strong hydrogen bonds, weak interactions such as, C–H···X (X = O, N, Cl), C–H···π and π···π stacking are also important in describing the self-assembly process in molecular solids [6,7]. Single crystal X-ray diffraction (SXRD) is generally the method of choice for determining crystal structures of molecular compounds and the study of intermolecular interactions in the solid state has focused on geometrical criteria such as, D(donor)···A(acceptor) distance and D–H···A angle that can be directly measured from the SXRD analysis [8,9]. With recent advances in the direct space approaches for structure solution [10–13], *ab-initio* crystal structure determination from powder X-ray diffraction

(PXRD) has been reported for organic systems with considerable molecular flexibility [14–17]. It should, however, be noted that structural crystallography with PXRD is significantly more challenging than that of its single crystal counterpart [18] because, first, the information content of a powder diffractogram is markedly lower, and second, it is far more difficult to extract structural information from a PXRD pattern due to systematic as well as random overlapping of peaks. This is reflected in the Cambridge Structural Database (version 5.37, update 2, CSD 2015 release) [19] search conducted among the organic compounds, which revealed that out of total 350196 entries only 1842 (~0.5%) structures have been solved from PXRD (including both laboratory and synchrotron X-ray data) without referring to an isotypic single crystal structure. Since structure determination from PXRD cannot establish the positions of hydrogen atoms unambiguously, consideration of geometrical criteria alone as obtained from the PXRD analysis without any supplementary evidence is unlikely to be reliable for assessing the hydrogen bonds. In this context, molecular electrostatic potential (MEP) [20–22] mapped onto a molecular surface can provide further insights into the nature of intermolecular interactions. This approach utilizes the calculated MEP surfaces around the molecule, in which the potential maxima and minima

* Corresponding author.

E-mail address: akm_ju@rediffmail.com (A.K. Mukherjee).

correspond to hydrogen bond donor and acceptor sites, respectively. Several attempts have been made relating MEP surfaces to crystal packing via intermolecular interactions [23–26].

In the current study we focus our attention to three oxime ether derivatives, (*E*)-3-methoxy-4-(prop-2-ynoxy)-benzaldehyde-*O*-prop-2-ynyl oxime (**2**), benzophenone-*O*-prop-2-ynyl oxime (**3**) and (*E*)-2-chloro-6-methylquinoline-3-carbaldehyde-*O*-prop-2-ynyl oxime (**1**) (Scheme 1). Since our attempts to grow single crystals suitable for X-ray analysis resulted in assemblies of microcrystals, structure determination of **3** and **4** was accomplished from PXRD analysis. To examine the contribution and influence of intermolecular interactions on crystal packing, the Hirshfeld surfaces [27], associated 2D fingerprint plots [28] and enrichment ratios [29] have been calculated for the listed compounds and some related systems retrieved from the CSD. The intermolecular interactions in **2–4** have been correlated with the MEP surface analysis. The study also includes electronic structures of **2–4** via DFT calculations. It should be noted that the present contribution is the second example of propargyloxime aldehyde/ketone after 2-methyl-*N*-(prop-2-yn-1-yloxy)-5,6-dihydro-1,3-benzothiazol-7(4H)-imine (COWXET) [19], available in the CSD.

2. Experimental section

2.1. Materials and general methods

All chemicals were obtained from commercial sources. Solvents were dried using standard methods, and chromatographic purification was performed using silica gel (100–200 mesh). Elemental analysis was carried out with a Perkin-Elmer 240C elemental analyzer. Fourier-transform infrared (FTIR) spectra were measured as KBr pellets using a Perkin-Elmer RX1 spectrometer. ¹H and ¹³C NMR spectra (300 MHz and 400 MHz) were recorded at 25 °C on a Varian-Gemini 300/400 MHz spectrometer using CDCl₃/DMSO-*d*₆ as solvent. Melting points were determined by open glass capillary method with a Sisco melting point apparatus and were uncorrected. Mass spectra were recorded on a HP 5989 instrument with electron ionization potential 70 eV. Reactions were monitored by thin layer chromatography (TLC) on pre-coated silica gel plates.

2.2. Synthesis

Primary oximes (**2b**, **3b** and **4b**) were synthesized by treating corresponding aldehydes (**2a** and **4a**, 1 mmol) or ketone (**3a**, 1 mmol) with hydroxyl amine hydrochloride (1.2 mmol) and sodium hydroxide (5 mmol) in ethanol (5 mL) at 25 °C followed by neutralization with acid. Crude oximes, thus obtained, were filtered and used without further purification. For the synthesis of compounds **2**, **3** and **4** (Scheme 2), equi-molar quantities of corresponding oximes (1 mmol of **2b**, **3b** and **4b**), anhydrous potassium carbonate (0.14 g, 1 mmol) and propargyl bromide (0.12 g, 1 mmol) were added to 15 mL of dry acetone and the resulting mixture was refluxed with vigorous magnetic stirring under anhydrous

atmosphere. The progress of reaction was monitored by checking TLC at regular intervals. After completion of reaction, acetone was distilled out followed by addition of water and the compounds were extracted with ethyl acetate (3 × 15 mL). The combined organic extracts were washed with 25 mL brine solution and dried over anhydrous sodium sulphate. The crude products were purified by column chromatography to yield microcrystalline powders of (*E*)-3-methoxy-4-(prop-2-ynoxy)-benzaldehyde-*O*-prop-2-ynyl oxime (C₁₄H₁₃NO₃) (**2**), benzophenone-*O*-prop-2-ynyl oxime (C₁₆H₁₃NO) (**3**) and (*E*)-2-chloro-6-methylquinoline-3-carbaldehyde-*O*-prop-2-ynyl oxime (C₁₄H₁₁ClN₂O) (**4**).

2.3. Spectroscopic data

2.3.1. (*E*)-3-Methoxy-4-(prop-2-ynoxy)-benzaldehyde-*O*-prop-2-ynyl oxime (C₁₄H₁₃NO₃) (**2**)

Colorless solid; yield 90%; mp 91(1) °C; mass (*m/z*) 243 (M⁺, 100%); ¹H NMR (400 MHz, CDCl₃): δ 8.07 (s, 1H), 7.27 (d, J 1.8 Hz, 1H), 7.06–7.00 (m, 2H), 4.79 (d, J 2.2 Hz, 2H), 4.77 (d, J 2.2 Hz, 2H), 3.93 (s, 3H), 2.54 (t, J 2.2 Hz, 1H), 2.52 (t, J 2.2 Hz, 1H); ¹³C NMR (100 MHz, DMSO-*d*₆): δ 149.7, 149.2, 148.3, 124.9, 120.9, 113.5, 109.0, 80.2, 78.9, 78.5, 77.4, 61.1, 55.9, 55.4; elemental analysis: found C 69.25, H 5.40, N 5.69%, calculated for C₁₄H₁₃NO₃: C 69.13, H 5.36, N 5.76%.

2.3.2. Benzophenone-*O*-prop-2-ynyl oxime (C₁₆H₁₃NO) (**3**)

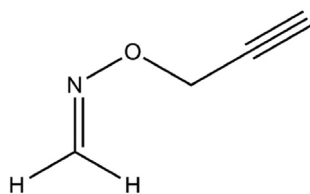
Colorless solid; yield 98%; mp 61(1) °C; mass (*m/z*) 236 (M⁺, 100%); ¹H NMR (400 MHz, CDCl₃): δ 7.51–7.49 (m, 2H), 7.44–7.41 (m, 3H), 7.39–7.25 (m, 5H), 4.76 (d, J 2.4 Hz, 2H), 2.46 (t, J 2.4 Hz, 1H), ¹³C NMR (100 MHz, CDCl₃): δ 158.3, 136.1, 132.9, 129.6, 129.0, 128.3, 80.0, 74.4, 61.9, IR (KBr) ν_{max}/cm⁻¹: 3283, 3063, 3029, 2919, 1493, 1444, 1424, 1355, 1328, 1053, 1003, 967, 922, 862, 773, 692; elemental analysis: found C 81.52, H 5.47, N 5.88%, calculated for C₁₆H₁₃NO: C 81.70, H 5.53, N 5.96%.

2.3.3. (*E*)-2-Chloro-6-methylquinoline-3-carbaldehyde-*O*-prop-2-ynyl oxime (C₁₄H₁₁ClN₂O) (**4**)

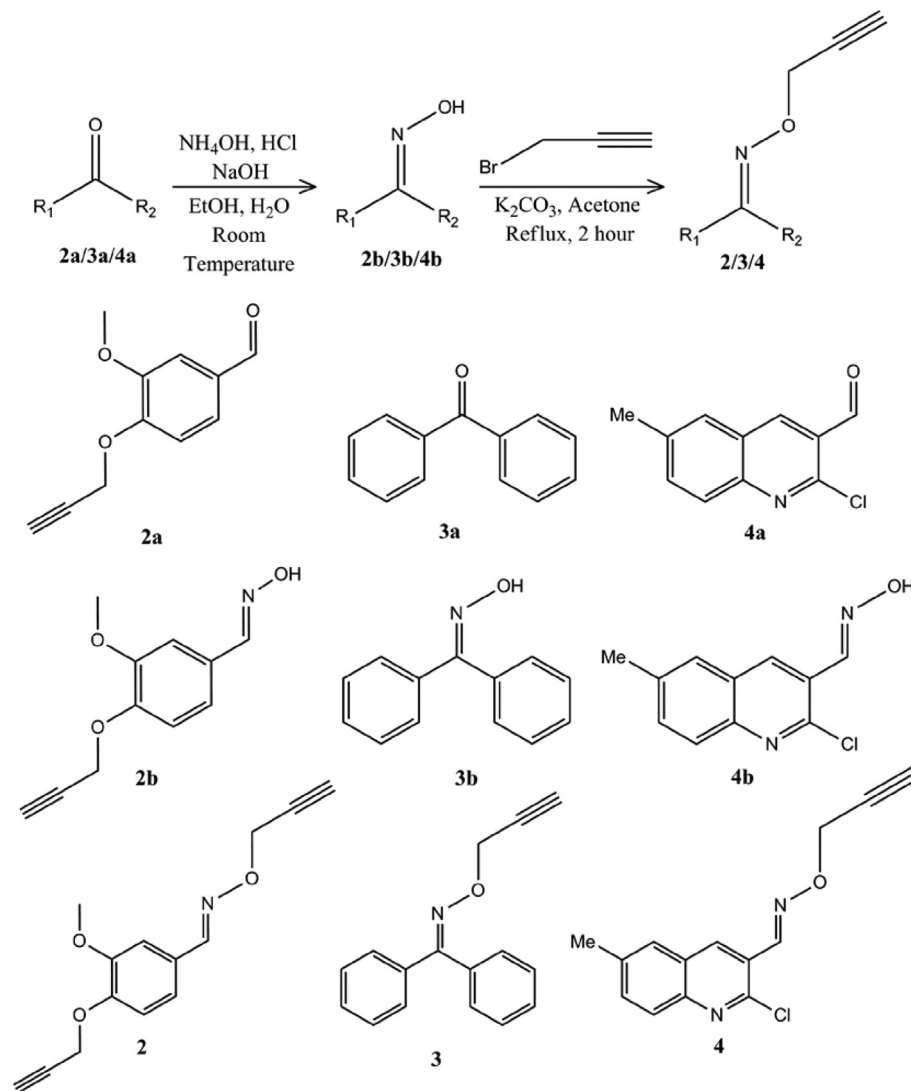
Colorless solid; yield 93%; mp 125(1) °C; mass (*m/z*) 259 (M⁺, 100%); ¹H NMR (400 MHz, CDCl₃): δ 8.61 (s, 1H), 8.60 (s, 1H), 7.89 (d, J 8.4 Hz, 1H), 7.61 (d, J 10.8 Hz, 1H), 7.58 (d, J 2.0 Hz, 1H), 4.85 (d, J 2.4 Hz, 2H), 2.56 (t, J 2.4 Hz, 1H), 2.18 (s, 3H); ¹³C NMR (100 MHz, CDCl₃): δ 148.0, 146.5, 146.4, 137.7, 135.3, 133.8, 127.9, 127.0, 126.8, 123.7, 79.1, 75.1, 62.2, 21.6, IR (KBr) ν_{max}/cm⁻¹: 3273, 3061, 2920, 1625, 1600, 1500, 1225, 1120, 830; elemental analysis: found C 64.91, H 4.19, N 10.88%, calculated for C₁₄H₁₁ClN₂O: C 65.00, H 4.26, N 10.83%.

2.4. Single crystal X-ray analysis of C₁₄H₁₃NO₃ (**2**)

Single crystal suitable for X-ray structure analysis was obtained by slow evaporation of a solution of **2** in a mixture of ethyl acetate and isopropyl alcohol (2:1). Intensity data were collected at 293(2) K on a Bruker Smart APEX II CCD area detector using graphite monochromated Mo Kα radiation (λ = 0.7107 Å). Data reduction was performed with SAINT [30] and an absorption correction was applied using SADABS [31]. The crystal structure was solved by direct methods with SHELXS97 [32] and refined using SHELXL97 [32] with anisotropic displacement parameters for all non-hydrogen atoms. The positions of hydrogen atoms were located from difference Fourier maps and refined with isotropic displacement parameters. The molecular view and crystal packing diagrams were generated using the Mercury (version 3.8) program [33]. Geometrical calculations were carried out with PLATON [34].



Scheme 1. Chemical diagram of formaldehyde *O*-prop-2-ynyl oxime (**1**).



Scheme 2. Synthesis of $C_{14}H_{13}NO_3$ (**2**), $C_{16}H_{13}NO$ (**3**) and $C_{14}H_{11}ClN_2O$ (**4**).

2.5. X-ray powder diffraction analysis of $C_{16}H_{13}NO$ (**3**) and $C_{14}H_{11}ClN_2O$ (**4**)

Powder X-ray diffraction (PXRD) data of **3** and **4** were recorded at ambient temperature [293(2) K] using a Bruker D8 Advance diffractometer operating in the Bragg–Brentano geometry, with $Cu\ K\alpha$ radiation ($\lambda = 1.5418\ \text{\AA}$). The PXRD patterns of **3** and **4** were indexed using EXPO 2014 [35] into monoclinic (in **3**) and triclinic (in **4**) unit cells. Given the volume of the unit cell and consideration of density, the number of formula units in the unit cell of **3** and **4** turned out as 4 (in **3**) and 2 (in **4**), respectively. Although the correct space group for **3** could not be assigned unambiguously on the basis of systematic absences, statistical analysis of PXRD data using the FINDSPACE module of EXPO 2014 [35] indicated probable space group as $P2_1/n$. The space group chosen for **4** was $P\bar{1}$. Structure solution of **3** and **4** was carried out by global optimization of structural models in direct space, based on a Monte-carlo search using the simulated annealing technique (in parallel tempering mode), as implemented in the program FOX [11]. The optimization of isolated molecules was performed using the energy gradient method as incorporated in MOPAC 9.0 [36].

The best solution (i.e., structure with the lowest R_{wp}) was used

as the initial structural models of **3** and **4** for Rietveld refinement [37], which was carried out using the GSAS program [38]. A pseudo-Voigt peak profile function was used during refinement and the background of the PXRD patterns of **3** and **4** was modeled by a shifted Chebyshev function of the first kind with 20 points regularly distributed over the entire 2θ range. The profile parameters were refined initially followed by the refinement of positional coordinates of all non-hydrogen atoms. Standard restraints were applied to bond lengths and bond angles, and planar restraints were used for phenyl and quinoline groups. While the refinement of a common isotropic displacement parameter (U_{iso}) for all non-hydrogen atoms in **4** was successful, the corresponding refinement of **3** diverged, which indicated possibility of wrong space group assignment. Structure solution of **3** was repeated in space group $P2_1$ with two molecules in the asymmetric unit and the refinement of common U_{iso} values for non-hydrogen atoms converged successfully in the non-centrosymmetric space group. Hydrogen atoms in molecules of **3** and **4** were placed in calculated positions with fixed U_{iso} values. In the final stages of refinement, a preferred orientation correction (generalised spherical harmonic model) was applied. The final Rietveld plots of **3** and **4** (Fig. 1) showed good agreement between the observed PXRD profile and

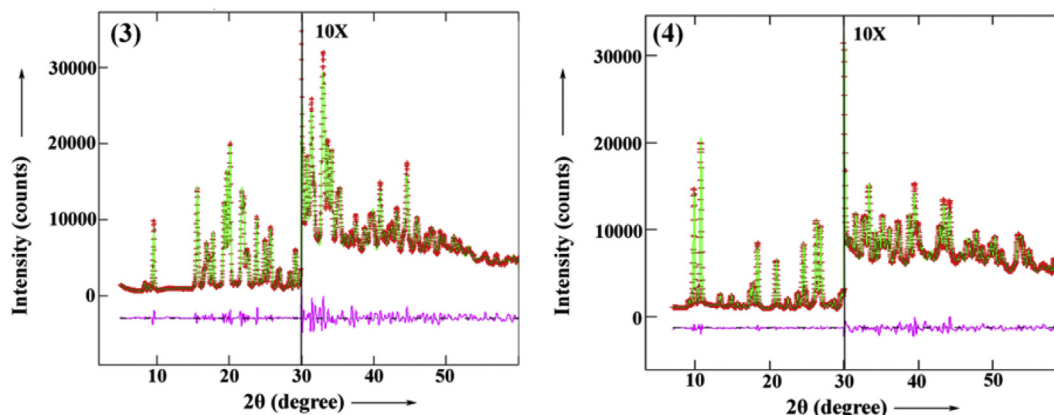


Fig. 1. Final Rietveld plots of $C_{16}H_{13}NO$ (3) and $C_{14}H_{11}ClN_2O$ (4). The intensity in the high angle region has been multiplied by a factor 10.

calculated powder diffraction pattern. The molecular views of **2–4** with atom labeling scheme are shown in Fig. 2. A summary of crystal data and relevant refinement parameters for **2–4** is listed in Table 1.

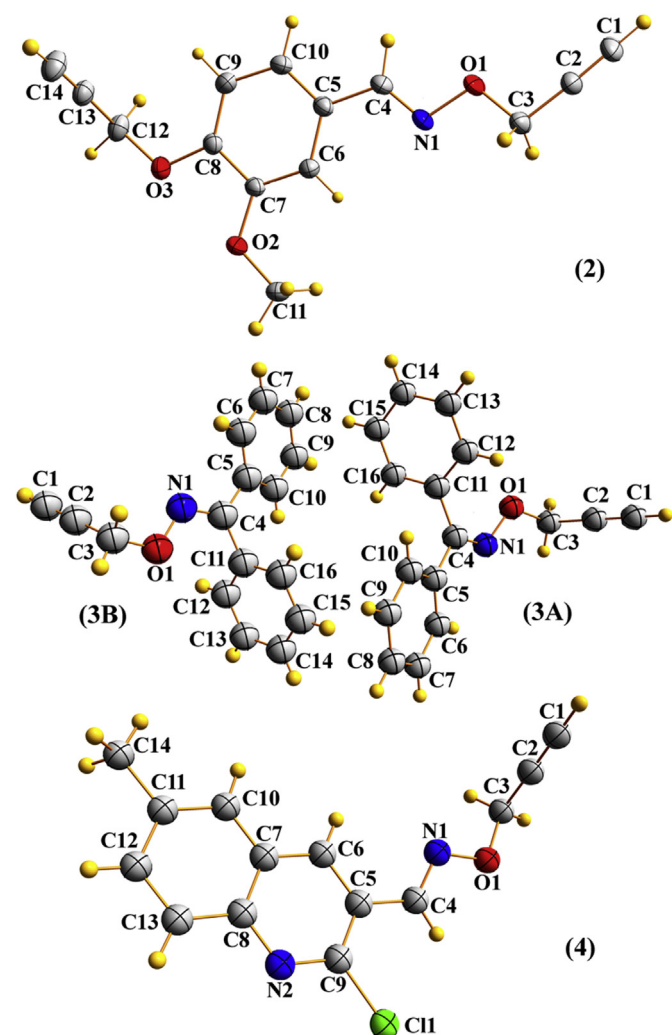


Fig. 2. Molecular views with atom labeling scheme for $C_{14}H_{13}NO_3$ (2), $C_{16}H_{13}NO$ (3) and $C_{14}H_{11}ClN_2O$ (4).

2.6. Hirshfeld surface analysis

The Hirshfeld surfaces [39] and associated 2D fingerprint plots [28] were calculated using Crystal Explorer [40]. Bond lengths to hydrogen atoms were set to typical neutron values ($C-H = 1.083 \text{ \AA}$ and $N-H = 1.009 \text{ \AA}$). For each point on the Hirshfeld isosurface, two distances d_e , the distance from the point to the nearest nucleus external to the surface, and d_i , the distance to the nearest nucleus internal to the surface, are defined. The normalized contact distance (d_{norm}) based on d_e and d_i is given by

$$d_{norm} = \frac{d_i - r_i^{vdW}}{r_i^{vdW}} + \frac{d_e - r_e^{vdW}}{r_e^{vdW}} \quad (1)$$

where r_i^{vdW} and r_e^{vdW} are the van der Waals radii of the atoms. The value of d_{norm} can be negative or positive depending on whether the intermolecular contacts are shorter or longer than the van der Waals separations. The parameter d_{norm} displays a surface with a red–white–blue color scheme, where the bright red spots highlight shorter contacts, the white areas represent contacts around the van der Waals separation, and the blue regions are devoid of close contacts.

2.7. Electrostatic potential calculation

The molecular electrostatic potential (MEP) is an effective tool for identifying and ranking the hydrogen bond donating and accepting sites in organic compounds [27,30]. The electrostatic potential at any point \vec{r} in the space surrounding a molecule can be expressed by

$$V(\vec{r}) = \sum_A \frac{Z_A}{|\vec{R}_A - \vec{r}|} - \int \frac{\rho(\vec{r}')}{|\vec{r} - \vec{r}'|} dr' \quad (2)$$

where Z_A is the charge of the nucleus A located at \vec{R}_A and $\rho(\vec{r})$ is the molecular electron density function. The sign of $V(\vec{r})$ at a particular region depends upon whether the effect of the nucleus or the electrons is dominant there. The MEP surfaces of **2–4** were generated with BLYP [41,42] correlation functional and a double numeric plus polarization (DNP) basis set using isolated molecule DFT calculations. All calculations including the electron densities and esp charges were carried out using the Dmol³ code [43]. The starting atomic coordinates for property calculations were obtained by geometry optimization of structures from the final X-ray

Table 1Crystal data and structure refinement parameters for $C_{14}H_{13}NO_3$ (**2**), $C_{16}H_{13}NO$ (**3**) and $C_{14}H_{11}ClN_2O$ (**4**).

	$C_{14}H_{13}NO_3$ (2)	$C_{16}H_{13}NO$ (3)	$C_{14}H_{11}ClN_2O$ (4)
Chemical formula	$C_{14}H_{13}NO_3$ (2)	$C_{16}H_{13}NO$ (3)	$C_{14}H_{11}ClN_2O$ (4)
Mol. Wt.	243.26	235.27	258.70
Temperature (K)	293(2)	293(2)	293(2)
Wavelength (Å)	0.7107	1.5418	1.5418
Crystal system	Monoclinic	Monoclinic	Triclinic
<i>a</i> (Å)	25.844(3)	20.0296(14)	6.9005(2)
<i>b</i> (Å)	4.1166(4)	5.9291(4)	9.9146(5)
<i>c</i> (Å)	24.109(3)	11.3749(7)	10.4540(5)
α (°)	90	90	109.628(2)
β (°)	95.531(3)	98.881(3)	95.317(4)
γ (°)	90	90	100.980(4)
Volume (Å ³)	2553.0(5)	1334.7(2)	651.8(1)
Space group, <i>Z</i>	C2/c, 8	P2 ₁ , 4	P $\bar{1}$, 2
Density (g/mL)	1.266	1.171	1.318
μ (mm ⁻¹)	0.090	0.577	2.503
<i>F</i> (000)	1024	496	268
Refinement	Full matrix least squares	Rietveld method	Rietveld method
2 θ range (°)	3.16 to 50.00	7.00 to 100.00	7.00 to 100.00
Largest peak and hole (e/Å ³)	0.180 and -0.173		
<i>R</i> ₁ (all data)/ <i>R</i> _p	0.0421	0.0430	0.0226
w <i>R</i> ₂ (all data)/ <i>R</i> _{wp} , <i>R</i> (<i>F</i> ²)	0.1207	0.0582, 0.0901	0.0309, 0.0639
GO <i>F</i> / χ^2	1.160	4.772	1.132

refinement cycles of **2–4** in the solid state with the same correlation functional and basis set. The dispersion correction was carried out with DFT-D approach using the TS scheme [44]. The electrostatic potentials were plotted on 0.017 au electron density isosurface [45]. The MEP surfaces have been mapped with a rainbow color scheme with red representing the highest negative potential region while blue representing the highest positive potential region.

3. Results and discussion

3.1. Structure description

In the title compounds (**2–4**), one hydrogen atom of the terminal CH₂ group of formaldehyde *O*-prop-2-ynyl oxime (**1**) has been replaced by a substituted phenyl ring in **2** and a chloromethylquinoline moiety in **4**, while in **3**, both CH₂ hydrogen atoms of **1** have been substituted by benzene rings. The *E* configuration of molecules has been established by the torsion angle O1-N1-C4-C5 of 177.3(1)° in **2** and -178.8(6)° in **4**. The linear propyne groups (C12-C14 atoms in **2** and C1-C3 atoms in **4**) are inclined to the planar cyclic fragment of molecules; the dihedral angle between the least-squares plane defined by C4-C10/O2/O3 atoms and the least-squares line through C12-C14 atoms in **2** is 57.0(1)°; the corresponding angle between the planar (C4-C14/N2/C11 atoms) and linear (C1-C3 atoms) fragments is 69.4(2)° in **4**. Two molecules (**A** and **B**) in the asymmetric unit of **3** are related by a pseudo inversion center about (0.243, 0.348, 0.252). A superposition of two molecules **A** and **B** in **3** (Fig. 3) reveals an almost identical conformation except the linear prop-2-ynyl fragment. This observation is consistent with the fact that although it was possible to obtain a model structure of **3** in the space group P2₁/n, the same could not be refined in the centrosymmetric space group (*U*_{iso} values of some of the non-hydrogen atoms were unrealistically large). The oxime-bridged phenyl rings in **3** are inclined to each other by 86.6(3)° in **A** and 89.1(3)° in **B**. The orientation of the prop-2-ynyl oxime moiety with respect to the benzene rings in **A** and **B** is established by the torsion angles O1A-N1A-C4A-C5A of -158.3(11)°, N1A-C4A-C5A-C6A of -19.6(11)°, O1B-N1B-C4B-C5B of 168.6(12)° and N1B-C4B-C5B-C6B of 30.3(15)°, respectively. An overlay of molecular conformations of **2–4** as determined by the X-ray analysis and theoretical calculations (solid state DFT) is shown in Fig. 4. The r.m.s. deviations between the geometrically optimized bond lengths,

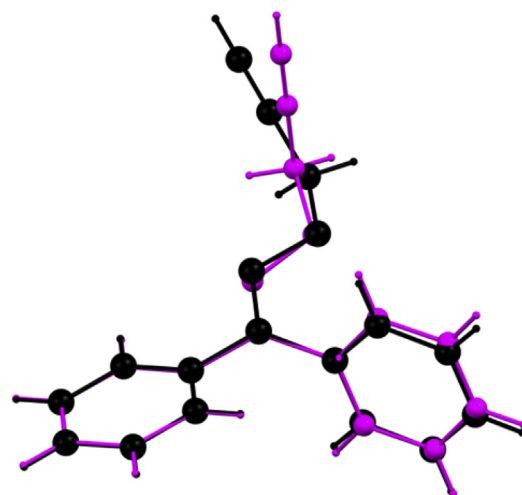


Fig. 3. Overlay of two molecules (pink: **A**, black: **B**) in the asymmetric unit of $C_{16}H_{13}NO$ (**3**). (For interpretation of the references to colour in this figure legend, the reader is referred to the web version of this article.)

bond angles (Table S1) and the corresponding crystallographically determined values are 0.02 Å, 0.5° in **2**, 0.02 Å, 1.7° in **3A/3B** and 0.03 Å, 2.2° in **4**. Close agreement between the X-ray analyzed structure and that obtained via quantum-mechanical calculations probably indicates that the compounds studied are stable conformers.

3.2. Crystal packing analysis

The crystal packing in **2–4** exhibits weak intermolecular C–H···O, C–H···N, C–H···Cl and C–H··· π hydrogen bonds and π ··· π interactions (Table 2). While the intermolecular C1–H1···O2 hydrogen bond connects molecules of **2** into a one-dimensional C₁(11) chain, the C14–H14···O1 hydrogen bonds form a spiral column along the [010] direction. The combination of polymeric chain and column generates a fused two-dimensional columnar structure propagating along the [1 $\bar{1}$ 0] direction in **2** (Fig. 5). The molecules **A** and **B** in the asymmetric unit of **3** are linked through C–H··· π hydrogen bonds (Table 2) to form a one-dimensional chain along

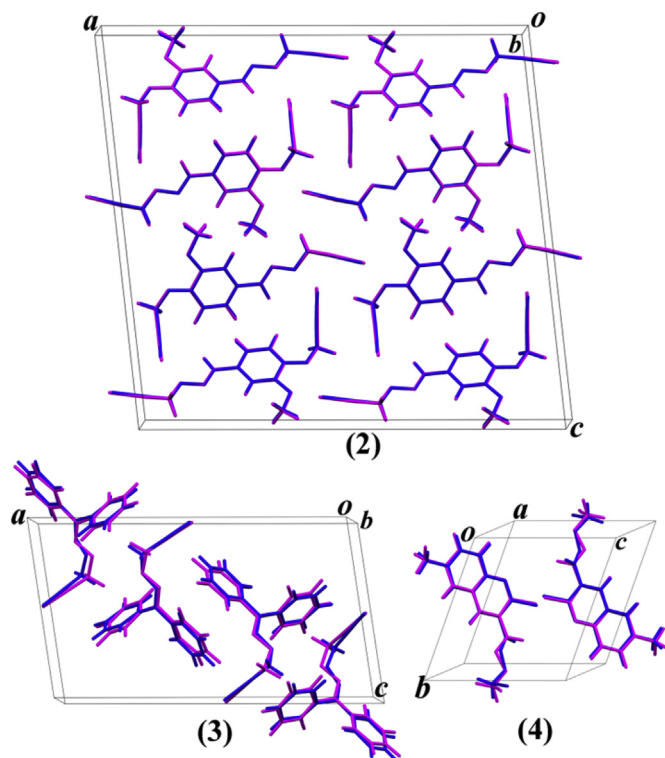


Fig. 4. Superposition of molecular conformations as obtained from X-ray structure analysis (blue) and solid state DFT calculation (magenta) for $C_{14}H_{13}NO_3$ (**2**), $C_{16}H_{13}NO$ (**3**) and $C_{14}H_{11}ClN_2O$ (**4**). (For interpretation of the references to colour in this figure legend, the reader is referred to the web version of this article.)

Table 2
Hydrogen bonds and $\pi \cdots \pi$ interactions in $C_{14}H_{13}NO_3$ (**2**), $C_{16}H_{13}NO$ (**3**) and $C_{14}H_{11}ClN_2O$ (**4**).

Interaction	D–H/Å	H···A/Å	D···A/Å	D–H···A/°	Symmetry code
$C_{14}H_{13}NO_3$ (2)					
C6–H6···N1	0.96(2)	2.63(2)	2.905(2)	97(1)	x, y, z
C1–H1···O2	0.94(2)	2.38(2)	3.278(2)	161(2)	1/2 + x, –1/2 + y, z
C14–H14···O1	0.89(2)	2.44(3)	3.251(2)	152(2)	1/2–x, 1/2 + y, 1/2–z
C1–H1···O3	0.94(2)	2.62(2)	3.380(2)	138(2)	1/2 + x, –1/2 + y, z
C12–H12B···O3	0.97(2)	2.71(2)	3.589(2)	151(1)	x, –1+y, z
$C_{16}H_{13}NO$ (3)					
C6A–H6A···N1A	0.93	2.59	2.883(15)	98	x, y, z
C6B–H6B···N1B	0.93	2.67	2.929(18)	97	x, y, z
C3A–H3A1···Cg(4)	0.93	2.90		158	x, y, –1+z
C3B–H3B1···Cg(2)	0.93	2.84		133	x, y, 1 + z
C15A–H15A···Cg(3)	0.93	2.99		154	x, y, z
C15B–H15B···Cg(1)	0.93	2.71		159	x, y, z
Cg(1) = C5A–C10A; Cg(2) = C11A–C16A; Cg(3) = C5B–C10B; Cg(4) = C11B–C16B					
$C_{14}H_{11}ClN_2O$ (4)					
C6–H6···N1	0.93	2.54	2.824(6)	98	x, y, z
C1–H1···N2	0.94	2.44	3.246(6)	144	–1+x, –1+y, z
C3–H3B···Cl1	0.95	2.81	3.537(4)	134	–x, –y, –z
Cg(1)···Cg(1)			3.836(1)		–x, 1–y, 1–z
Cg(1)···Cg(1)			3.896(1)		1–x, 1–y, 1–z
Cg(1)···Cg(2)			3.732(1)		–x, 1–y, 1–z
Cg(1)···Cg(2)			3.953(1)		1–x, 1–y, 1–z
Cg(1): N2, C5–C9 atoms; Cg(2): C7, C8, C10–C13 atoms					

the [001] direction (Fig. 6). In **4**, the centrosymmetrically related molecules are joined via pair of C–H···Cl hydrogen bonds forming a cyclic ring with an $R_2^2(16)$ graph-set motif [46]. The propagation of $R_2^2(16)$ synthon through intermolecular C1–H1···N2 hydrogen bonds generates a one-dimensional chain with fused $R_2^2(16)$ and $R_4^4(16)$ rings along the [110] direction (Fig. 7). The chains in **4** are weakly linked by aromatic $\pi \cdots \pi$ interactions (Table 2) into a three-

dimensional framework. The interplanar spacing between parallel quinoline rings (C5–C13, N2 atoms) is 3.539(1) Å with ring-centroid separations for two heterocyclic six-membered rings (P: C5–C9, N2 atoms) of 3.896(1) Å, and between ring P and phenyl moiety (Q: C7, C8, C10–C13 atoms) of 3.953(1) Å. The corresponding centroid offset values for P:P and P:Q are 1.629 Å and 1.761 Å, respectively. The Hirshfeld surfaces of **2–4** are illustrated in Fig. 8. The red spots labeled as ‘a/a’ in Fig. 8(i) and ‘b’ in Fig. 8(ii) are due to C–H···O (in **2**) and C–H···N (in **4**) hydrogen bonds. Other visible red patches (c/c’) in Fig. 8(ii) correspond to C–H···Cl interaction in **4**. The Hirshfeld surfaces for molecules **A** and **B** in **3**, Fig. 8(iii), are devoid of any significant red spots, which is consistent with Table 2 showing only weak C–H··· π interactions. In the 2D fingerprint plot, Fig. 9(i), two sharp spikes (‘a’ and ‘a’) of almost equal length in the region $2.2 < d_e + d_i < 2.6$ Å are characteristic of C1–H1···O2 bonded C₁(11) chain in **2**. The spikes due to C14–H14···O1 hydrogen bond in **2** are masked within the spikes a/a’ in Fig. 9(i). The corresponding C1–H1···N2 interactions in **4** appear as sharp spikes (labeled as ‘b’ and ‘b’) in the region $2.3 < d_e + d_i < 2.8$ Å in Fig. 9(ii). Additional spikes (‘c’ and ‘c’) in Fig. 9(ii) are attributable to the C–H···Cl interaction in **4**. An intense green patch in the central part of Fig. 9(ii) represents $\pi \cdots \pi$ interactions [27] in **4**. Lack of any C/N–H···O hydrogen bond in **3** is reflected in the absence of sharp spike in Fig. 9(iii). The wings marked with black circles in Fig. 9(iii) represent the C–H··· π interactions in **3A** and **3B**. The intermolecular H···H contacts comprising of 50.7% in **3A** and 52.4% in **3B** of the total number of contacts, are major contributors to the crystal packing in **3**. This is reflected by the central spikes extending up to (d_i, d_e) region of (1.0 Å, 1.0 Å) in **3A** and **3B**.

The enrichment ratio (E) [29], which is defined as the ratio between the proportion of actual contacts in the crystal and the

theoretical proportion of random contacts, has been determined for the intermolecular contacts in **2**, **3** (for two independent molecules **A** and **B**) and **4** (Table S2) to study the propensity of two chemical species to be in contact. The value of E is greater than unity for pair of elements with higher propensity to form contacts, while pairs which tend to avoid contacts yield E values less than unity. In **2**, the total Hirshfeld surface area is dominated by H···H and H···C

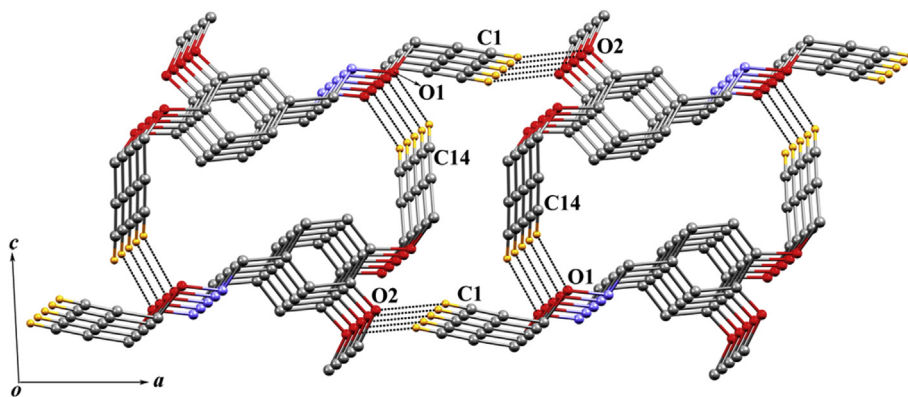


Fig. 5. Two dimensional columnar architecture formed by C–H...O hydrogen bonds in $C_{14}H_{13}NO_3$ (**2**).

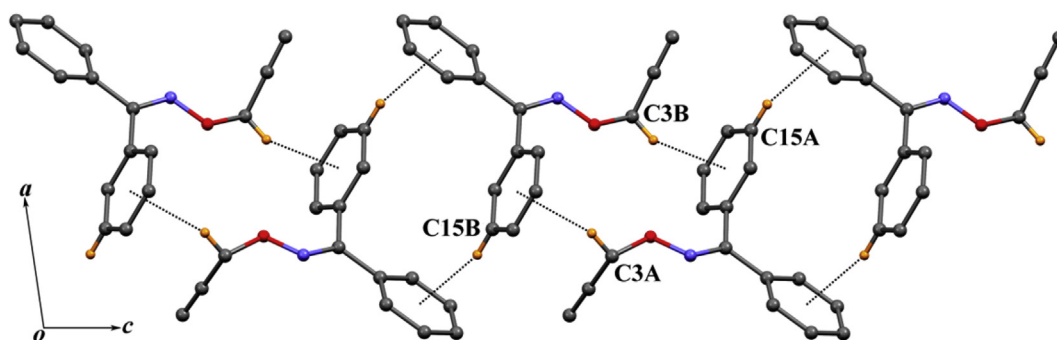


Fig. 6. One dimensional molecular ribbon formed by C–H... π hydrogen bonds in $C_{16}H_{13}NO$ (**3**).

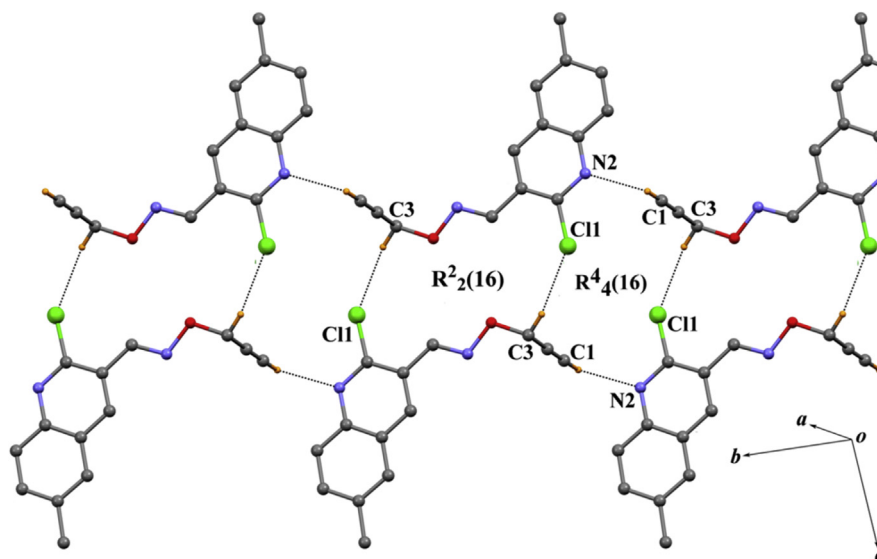


Fig. 7. One dimensional molecular chain formed by C–H...N and C–H...Cl hydrogen bonds in $C_{14}H_{11}ClN_2O$ (**4**).

contacts, comprising of 38.4% and 33.9%, respectively. The corresponding enrichment ratios, however, show an increased propensity of H...C contacts to form ($E_{HC} = 1.15$), and the H...H contacts are less favored ($E_{HH} = 0.88$). It should be noted that H...O contacts are more favored in **2** ($E_{HO} = 1.35$). This is consistent with the crystallographic results showing all three oxygen atoms (O1–O3) participating in intermolecular hydrogen bond in **2** (Table 2).

The E_{HH} values of 0.90 in **3A** and 0.91 in **3B**, indicate an almost

identical propensity to form H...H contacts for two crystallographically independent molecules in **3**, and these contacts contribute about 50% of the total Hirshfeld surface (Fig. 10). Slightly increased propensity to form H...C and H...N contacts has been observed in **3A** ($E_{HC} = 1.29$ and $E_{HN} = 1.26$) compared to that in **3B** ($E_{HC} = 1.27$ and $E_{HN} = 1.23$). This can be attributed to marginally higher percentage of H...C and H...N contacts to the total surface area in **3A** than in **3B**, and an almost identical random contacts for

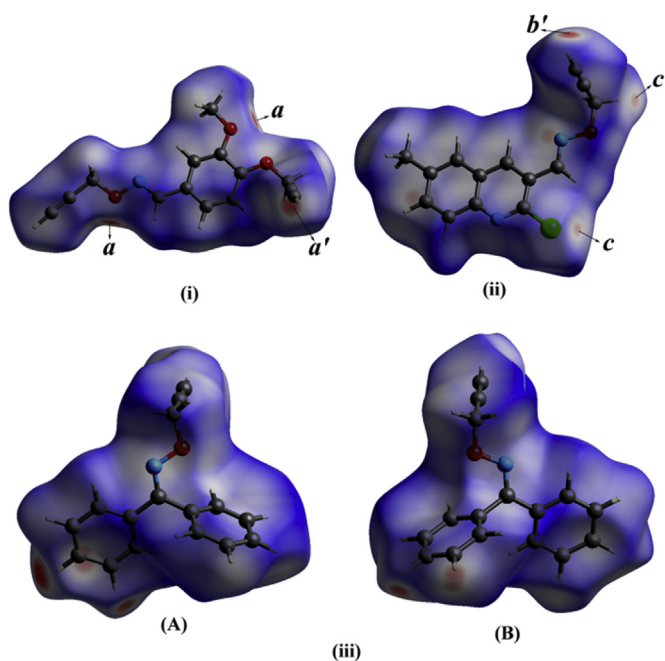


Fig. 8. Hirshfeld surfaces of (i) $C_{14}H_{13}NO_3$ (**2**), (ii) $C_{14}H_{11}ClN_2O$ (**4**) and (iii) $C_{16}H_{13}NO$ (**3**).

both molecules in **3**. The E_{HO} values for two independent molecules in **3** with identical random contacts ($R_{HO} = 3.3\%$) are larger than unity (1.36 and 1.33), indicating that $H\cdots O$ contacts have an increased propensity to form. The distribution of main intermolecular contacts on the total Hirshfeld surface area of **4** is similar viz. $H\cdots C$ (18.9%), $H\cdots Cl$ (15.7%), $C\cdots C$ (10.8%), $H\cdots N$ (10.0%) and $H\cdots O$ (6.2%) except $H\cdots H$ contacts, which appear to be the major contributor (34.9%). The enrichment ratios reveal that $H\cdots H$ ($E_{HH} = 0.96$), $H\cdots N$ ($E_{HN} = 1.35$), $H\cdots Cl$ ($E_{HCl} = 1.51$) and $H\cdots O$ ($E_{HO} = 1.68$) contacts are more favored, and $C\cdots C$ contacts with $E_{CC} = 2.25$ are even more favored in **4**. High enrichment ratio for $C\cdots C$ contacts ($E_{CC} = 2.25$) is a consequence of several $\pi\cdots\pi$ interactions in **4** (Table 2).

The relative contribution of different interactions to the Hirshfeld surfaces of **2–4** as well as a few closely related oxime derivatives (Tables S3–S9) retrieved from the CSD such as, (E)-4-hydroxy-3-methoxybenzaldehyde oxime (VIMRUE) [47], (E)-phenyl(*m*-tolyl) methanone O-methyl oxime (HIFYIG) [48], benzophenone oxime (XULKUK) [19] and 6-chloro-3-ethyl-4-isobutylisoxazolo [4,5-*c*] quinoline (NOLCUN) [49] is shown in Fig. 10. Due to replacement of both hydroxyl H atoms in VIMRUE by propargyl ($-CH_2CCH$) groups in **2**, the $H\cdots O$ contribution to the Hirshfeld surface reduces from 23.0% in VIMRUE to 15.8% in **2** with a corresponding increase in the $H\cdots C$ interactions from 18.8% in VIMRUE to 33.9% in **2**. The compound **3** bears a close structural resemblance with benzophenone oxime (XULKUK). With different substitutions in the XULKUK skeleton, a

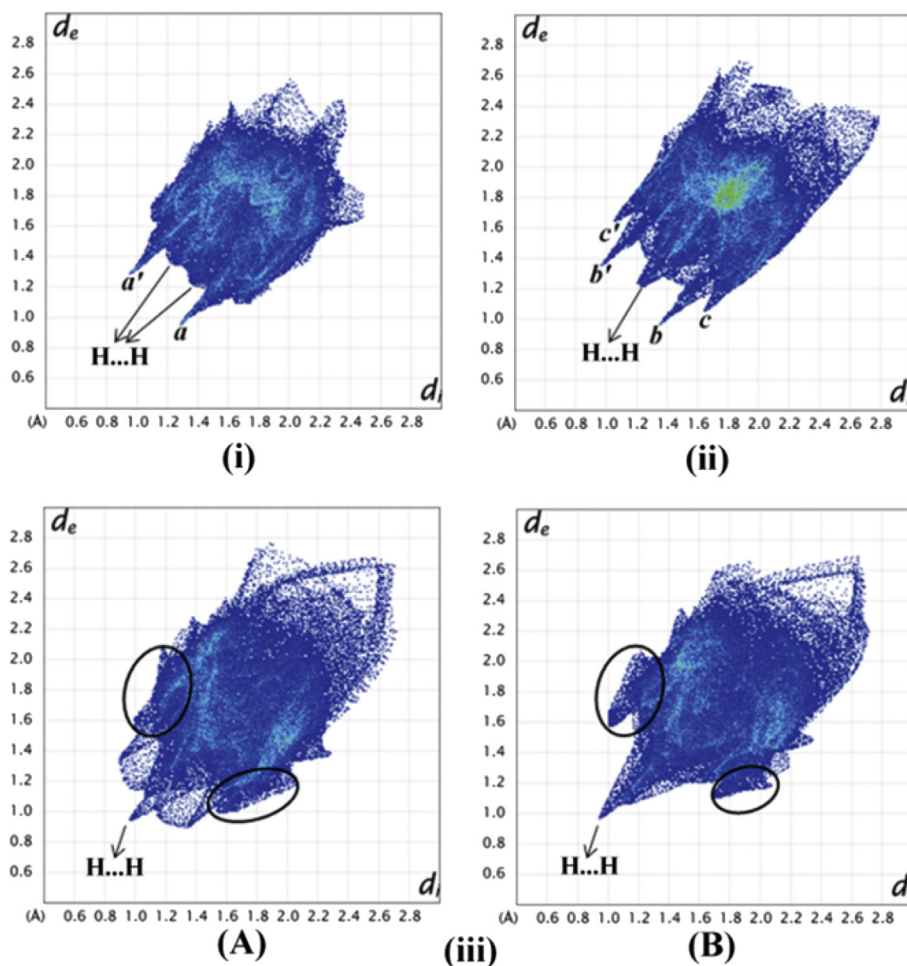


Fig. 9. Fingerprint plots of (i) $C_{14}H_{13}NO_3$ (**2**), (ii) $C_{14}H_{11}ClN_2O$ (**4**) and (iii) $C_{16}H_{13}NO$ (**3**).

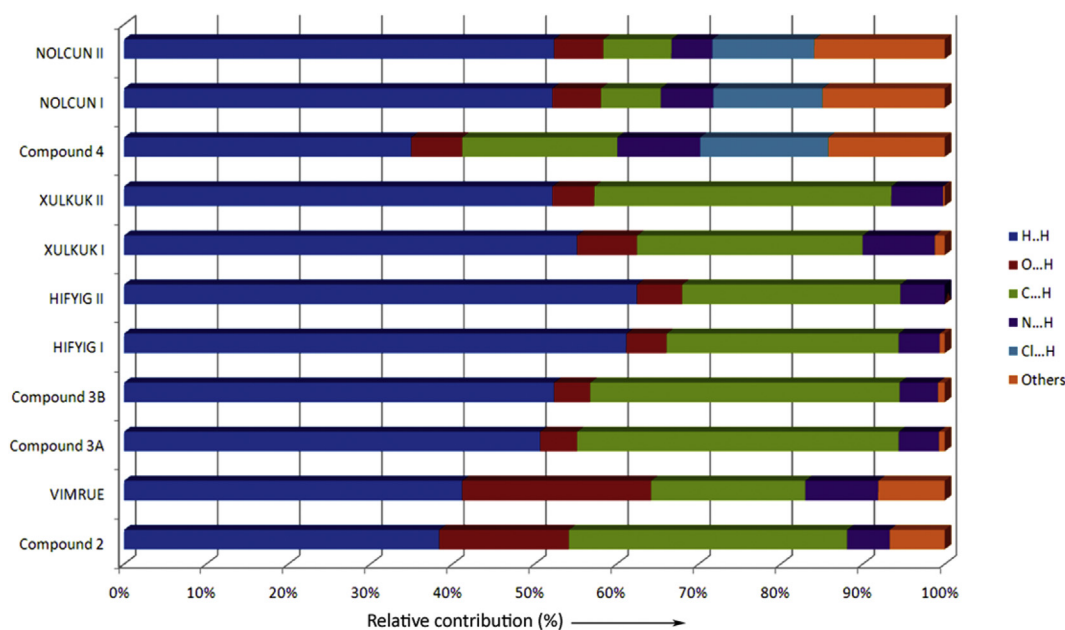


Fig. 10. Relative contribution of different interactions to the Hirshfeld surfaces of $C_{14}H_{13}NO_3$ (**2**), $C_{16}H_{13}NO$ (**3**) and $C_{14}H_{11}ClN_2O$ (**4**) and a few related structures from the CSD.

propargyl group replacing the hydroxyl H atom of XULKUK in **3** and that a methyl group in HIFYIG, the molecular interactions are predominantly of H...H and H...C types, which can account for about 85% (82.7–88.4% in XULKUK, 89.2–90.1% in **3**, and 89.1–89.5% in HIFYIG) of the Hirshfeld surface area. Incidentally, these three benzophenoneoxime compounds crystallized with $Z' = 2$.

3.3. Molecular electrostatic potential

The MEP surfaces of **2–4** (Fig. 11) have been analyzed in terms of intra- and inter-molecular hydrogen bonds. The MEP derived charges with the density functional BLYP using DMol³ program indicated negative charges on the oxygen (O1–O3) and nitrogen (N1 and N2) atoms. The terminal H atoms of the propargyl group (H1,

H14 in **2**, H1A in **3A**, H1B in **3B** and H1 in **4**) carry most positive charge among the hydrogen atoms due to electron withdrawing nature of adjacent alkyne carbon atoms. Due to this charge redistribution, the dipole moments of **2**, **3A**, **3B** and **4** are 0.57, 0.32, 0.29 and 1.57 a.u., respectively. The electrostatic potential maxima and minima ($V_{s,max}$, $V_{s,min}$) associated with different donor and acceptor atoms can serve as good indicators of hydrogen bond validation in **2–4**. While the alkyne hydrogen atoms in **2** (H1 and H14) are associated with two most positive potential values of 45 and 40 kcal/mol, respectively, the phenoxy O2 and O3 atoms correspond to the maximum negative potential of -40 kcal/mol. Other relatively high positive/negative potentials in **2** around H12A (31 kcal/mol), H12B (30 kcal/mol) and N1 (-28 kcal/mol) atoms are attributable to intra/intermolecular interactions involving these atoms. This is consistent with hydrogen bonds in **2** (Table 2) obtained via crystallographic analysis. In **3**, the two most negative potentials ($V_{s,min}$) associated with molecules 3A (-35 kcal/mol for N1A and -32 kcal/mol for O1A) and 3B (-34 kcal/mol for N1B and -32 kcal/mol for O1B) are due to intramolecular C–H...O and C–H...N interactions. The corresponding positive potentials ($V_{s,max}$) around the hydrogen atoms involved in intramolecular interactions are 21, 20, 18 and 18 kcal/mol for H3B2, H3A2, H12A and H12B, respectively. The presence of negative potentials associated with centers of phenyl rings viz, C5A–C10A (-16 kcal/mol), C11A–C16A (-20 kcal/mol), C5B–C10B (-16 kcal/mol), C11B–C16B (-19 kcal/mol) and H3A1 (26 kcal/mol), H3B1 (25 kcal/mol), H15A (22 kcal/mol), H15B (22 kcal/mol) can be rationalized in terms of C–H ... π interactions in **3**. It should, however, be noted that the alkyne hydrogen atom (H1A and H1B) in both molecules of **3** with highest positive potential of 39 kcal/mol for **3A** and **3B** does not participate in hydrogen bond. In **4**, the hydrogen bond acceptor is characterized by the most negative potential around the quinoline N2 atom (-39 kcal/mol) and the corresponding donor atom (alkyne H1) is linked with the maximum positive potential of 43 kcal/mol. The relatively moderate negative potentials around O1 (-24 kcal/mol) and N1 (-22 kcal/mol) atoms are due to intramolecular hydrogen bonds in **4**. The chlorine atom (Cl1) in **4**, associated with slightly negative potential (-4 kcal/mol), acts as a weak acceptor and forms weak intermolecular interaction with

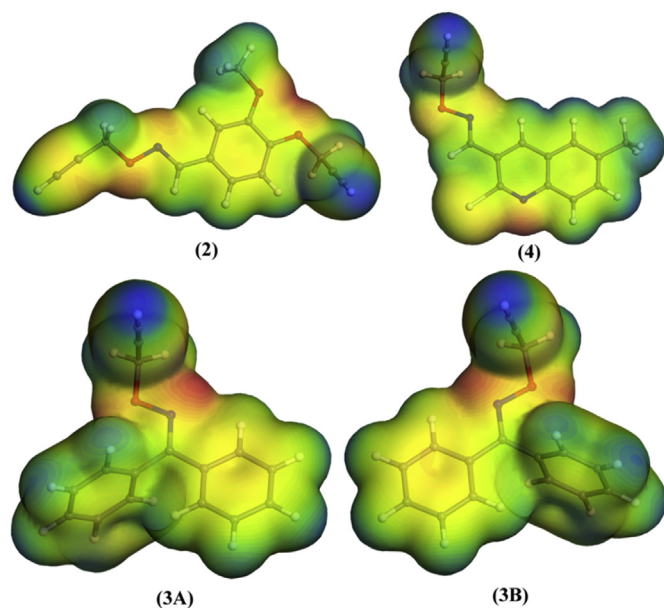


Fig. 11. MEP surfaces of $C_{14}H_{13}NO_3$ (**2**), $C_{16}H_{13}NO$ (**3**) and $C_{14}H_{11}ClN_2O$ (**4**).

H3B; the corresponding positive potential around H3B atom is 29 kcal/mol (Table S10).

3.4. Electronic structure

The frontier molecular orbitals HOMO (highest occupied molecular orbital), LUMO (lowest unoccupied molecular orbital), HOMO-1 (second highest occupied molecular orbital) and LUMO+1 (second lowest unoccupied state) of **2–4** are depicted in Fig. 12, where colors on the isosurface are to distinguish the phase of the wave function. These frontier orbitals are the most involved states in electronic transitions. With substituted phenyl (in **2**) and quinoline (in **4**) rings replacing one of the hydrogen atoms of the CH₂ group in formaldehyde *O*-prop-2-ynyl oxime (**1**) skeleton, the HOMO electrons in **2–4** are mostly localized on the oxygen (O1–O3 in **2** and O1 in **4**) and quinoline nitrogen (N2 in **4**) atoms in addition to the C–C bonds of the aromatic rings showing bonding-antibonding patterns characteristic of a π -conjugated ring system. The occupied levels have a bonding character on the C4–N1 double bond. The prop-2-ynyl chain (–CH₂–C \equiv CH) in **2–4** had hardly any HOMO or LUMO population. The LUMO level in **2** and **4** has more contributions to the N1 atom, C4–C5 bond as well as the ring atoms (C6, C8, C10 in **2** and N2, C6, C8, C10, C12, C13 in **4**). In **3**, both hydrogen atoms of the CH₂ group in **1** have been replaced by phenyl rings, thus making the molecule approximately symmetric about the C4–N1 bond. The frontier orbitals of **3** shown in Fig. 12 indicate that the LUMO and LUMO+1 levels are located on the N1

atom, adjacent C–C bond and the two benzene rings, while the HOMO and HOMO-1 level contributions are on the O1 atom and N1–C4 bond in addition to the phenyl rings. A striking feature in the electronic structure of **3** is the occurrence of almost degenerate states for both HOMO and LUMO levels. Since no symmetry constraints are imposed in such a large molecular structure, both HOMO and LUMO levels can be considered degenerate [50]. This reflects the fact that the inherent symmetry is preserved and the energy levels are not split. Consequently a higher HOMO-LUMO gap is expected for **3** than that of **2** and **4**.

Energy eigen values E_{HOMO} and E_{LUMO} calculated using a BLYP correlation functional are –4.71 and –1.74 eV in **2**, –5.16 and –1.82 eV in **3** and –5.51 and –2.78 eV in **4**, which indicate that the energy gap of 3.34 eV in **3** as the highest among the three oxime ether derivatives. It is widely accepted that the energy difference between HOMO and LUMO can be considered as a rough estimate of band gap i.e. the transition energy required to excite electrons from the ground state to the first dipole-allowed excited state [51,52]. The band gap in **3** with both aldehyde hydrogen atoms of formaldehyde *O*-prop-2-ynyl oxime (**1**) being substituted by two benzene rings is higher by 0.37 eV/0.61 eV than that of **2** and **4**, in which only one aldehyde hydrogen atom of **1** has been replaced by a substituted phenyl or quinoline moiety. This behavior is consistent with the expected higher reactivity of aldoximes compared to ketoximes [53]. The chemical potential (μ), expressed as $\mu = (E_{\text{HOMO}} + E_{\text{LUMO}})/2$, is –3.2, –3.5 and –4.1 eV for **2**, **3** and **4**, respectively. High HOMO-LUMO energy difference and negative μ

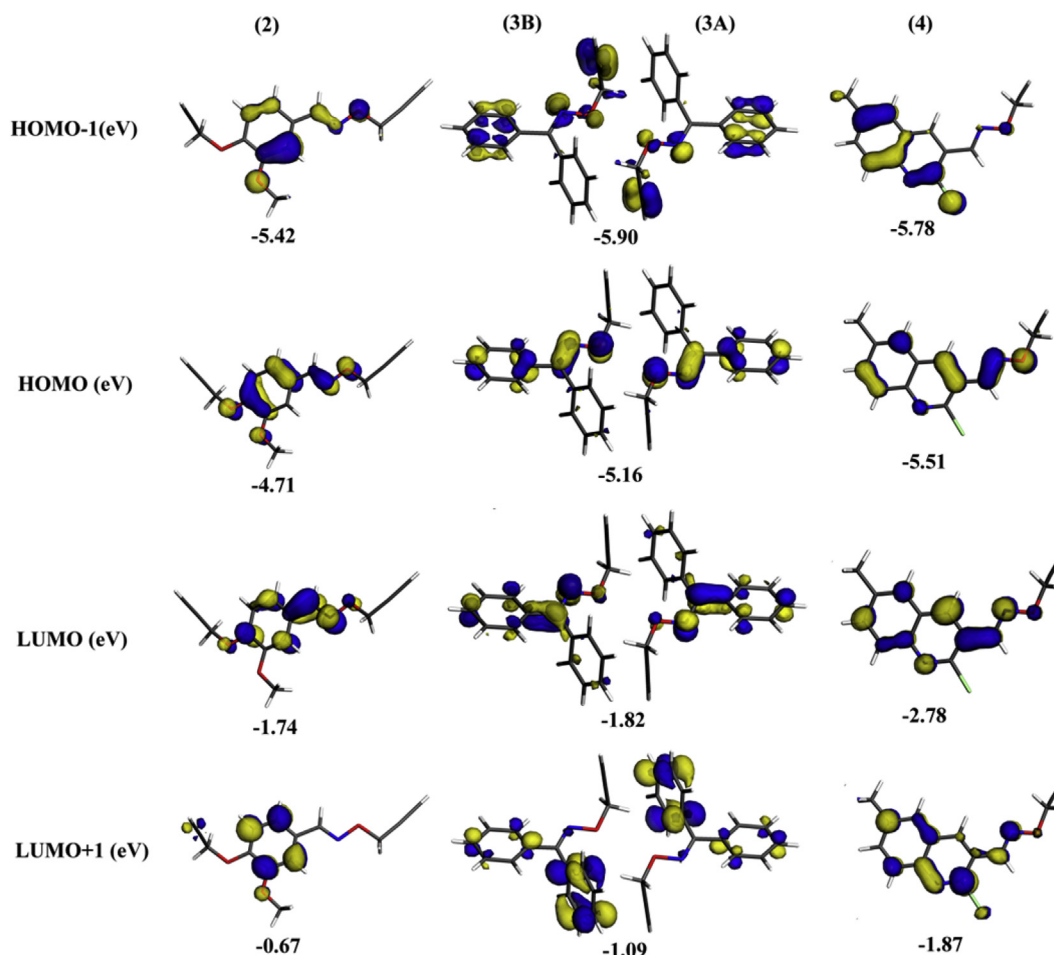


Fig. 12. Molecular orbitals of C₁₄H₁₃NO₃ (**2**), C₁₆H₁₃NO (**3**) and C₁₄H₁₁ClN₂O (**4**).

values of 2–4 indicate that the compounds are stable.

4. Conclusions

In summary, three aldoxime and ketoxime derivatives (2–4) of formaldehyde *O*-prop-2-ynyl oxime (1) have been synthesized and structurally characterized. The potential of direct space methodology for solving crystal structures of molecular compounds is highlighted. The subtleties of crystal packing in the compounds are illustrated by a variation of substitution in formaldehyde *O*-prop-2-ynyl oxime skeleton, which assemble molecules into a two-dimensional columnar architecture in 2, a one-dimensional molecular ribbon in 3 and a three-dimensional framework in 4. Hirshfeld surface analysis of 2, 3 and a few related oxime ether derivatives showed that the structures are mainly characterized by H···H, H···C and H···O contacts, whereas in 4, some contribution from H···N and H···Cl contacts is clearly observed. The results also emphasize that intermolecular interactions, in particular, weak hydrogen bonds can be rationalized using the molecular electrostatic potential (MEP) calculation. The estimated higher band gap (ΔE) in 3 compared to that of 2 and 4 is consistent with the general trend that ketoxime (3) is more stable than aldoximes (2 and 4). The present work facilitates our understanding of how different substitutions in formaldehyde *O*-prop-2-ynyl oxime skeleton can influence the overall intermolecular interactions leading to different supramolecular assemblies in the solid state.

Acknowledgements

The authors thank Mr. Rajdip Roy, Department of Organic Chemistry, IACS, Kolkata-700032, India, for helping in single crystal X-ray data collection of 2. Financial support from the Council for Scientific and Industrial Research, New Delhi, India, for a senior research fellowship (SRF) to T.D. [grant no. 09/096(0755)/2012-EMR-I] is gratefully acknowledged.

Appendix A. Supplementary data

Supplementary data associated with this article can be found in the online version, at <http://dx.doi.org/10.1016/j.molstruc.2017.02.089>. These data include MOL files and InChIKeys of the most important compounds described in this article.

References

- [1] T. Steiner, *Angew. Chem. Int. Ed.* 41 (2002) 48–76.
- [2] G.R. Desiraju, *Crystal engineering: the Design of Organic Solids*, Elsevier, New York, 1989.
- [3] G.A. Jeffrey, W. Saenger, *Hydrogen Bonding in Biological Structures*, Springer-Verlag, Berlin, 1991.
- [4] G.R. Desiraju, *Nature* 412 (2001) 397–400.
- [5] F.H. Allen, W.D.S. Motherwell, P.R. Raithby, G.P. Shields, R. Taylor, *New J. Chem.* 23 (1999) 25–34.
- [6] G.R. Desiraju, T. Steiner, *The Weak Hydrogen Bond*, Oxford University Press, New York, 2001.
- [7] B. Moulton, M.J. Zaworotko, *Chem. Rev.* 101 (2001) 1629–1658.
- [8] G.A. Jeffrey, *An Introduction to Hydrogen Bonding*, Oxford University Press, New York, 1997.
- [9] D. Braga, F. Grepioni, K. Biradha, V.R. Pedireddi, G.R. Desiraju, *J. Am. Chem. Soc.* 117 (1995) 3156–3166.
- [10] W.I.F. David, K. Shankland, *Acta Crystallogr. Sect. A* 64 (2008) 52–64.
- [11] V. Favre-Nicolin, R. Černý, Z. Krist. - *Cryst. Mat.* 219 (2004) 847–856.
- [12] S. Pagola, P.W. Stephens, D.S. Bohle, A.D. Kosar, S.K. Madsen, *Nature* 404 (2000) 307–310.
- [13] K.D.M. Harris, E.Y. Cheung, *Chem. Soc. Rev.* 33 (2004) 526–538.
- [14] T. Dey, P. Chatterjee, A. Bhattacharya, S. Pal, A.K. Mukherjee, *Cryst. Growth Des.* 16 (2016) 1442–1452.
- [15] U. Das, J. Naskar, A.K. Mukherjee, *J. Pept. Sci.* 21 (2015) 845–852.
- [16] P.A. Williams, C.E. Hughes, K.D.M. Harris, *Angew. Chem. Int. Ed.* 54 (2015) 3973–3977.
- [17] J.-B. Arlin, R.M. Bhardwaj, A. Johnston, G.J. Miller, J. Bardin, F. MacDougall, P. Fernandes, K. Shankland, W.I.F. David, A.J. Florence, *CrystEngComm* 16 (2014) 8197–8204.
- [18] K.D.M. Harris, M. Tremayne, B.M. Kariuki, *Angew. Chem. Int. Ed.* 40 (2001) 1626–1651.
- [19] C.R. Groom, I.J. Bruno, M.P. Lightfoot, S.C. Ward, *Acta Crystallogr. Sect. B* 72 (2016) 171–179.
- [20] C.A. Hunter, *Angew. Chem. Int. Ed.* 43 (2004) 5310–5324.
- [21] D. Musumeci, C.A. Hunter, R. Prohens, S. Scuderi, J.F. McCabe, *Chem. Sci.* 2 (2011) 883–890.
- [22] P. Politzer, J.S. Murray, *Cryst. Growth Des.* 15 (2015) 3767–3774.
- [23] J.S. Murray, P. Politzer, *J. Org. Chem.* 56 (1991) 6715–6717.
- [24] F.A. Bulat, A. Toro-Labbe, T. Brinck, J.S. Murray, P. Politzer, *J. Mol. Model.* 16 (2010) 1679–1691.
- [25] C.B. Aakeröy, T.K. Wijethunga, J. Desper, *New J. Chem.* 39 (2015) 822–828.
- [26] C.B. Aakeröy, K. Epa, S. Forbes, N. Schultheiss, J. Desper, *Chem. Eur. J.* 19 (2013) 14998–15003.
- [27] M.A. Spackman, D. Jayatilaka, *CrystEngComm* 11 (2009) 19–32.
- [28] M.A. Spackman, J.J. McKinnon, *CrystEngComm* 4 (2002) 378–392.
- [29] C. Jelsch, K. Ejsmont, L. Huder, *IUCr* 1 (2014) 119–128.
- [30] APEX2, SAINT and XPREP, Bruker AXS Inc, Madison, Wisconsin, USA, 2007.
- [31] SADABS, Bruker AXS Inc, Madison, Wisconsin, USA, 2001.
- [32] G. Sheldrick, *Acta Crystallogr. Sect. A* 64 (2008) 112–122.
- [33] C.F. Macrae, P.R. Edgington, P. McCabe, E. Pidcock, G.P. Shields, R. Taylor, M. Towler, J. van de Streek, *J. Appl. Crystallogr.* 39 (2006) 453–457.
- [34] A.L. Spek, *Acta Crystallogr. Sect. D* 65 (2009) 148–155.
- [35] A. Altomare, C. Cuocci, C. Giacovazzo, A. Moliterni, R. Rizzi, N. Corriero, A. Falcicchio, *J. Appl. Crystallogr.* 46 (2013) 1231–1235.
- [36] J.J.P. Stewart, *J. Mol. Model.* 13 (2007) 1173–1213.
- [37] H. Rietveld, *Acta Crystallogr.* 22 (1967) 151–152.
- [38] A.C. Larson, R.B. Von Dreele, *General Structure Analysis System (GSAS)*, Los Alamos Laboratory Report, LAUR, 2000, 86–748.
- [39] J.J. McKinnon, D. Jayatilaka, M.A. Spackman, *Chem. Commun.* (2007) 3814–3816.
- [40] S.K. Wolff, D.J. Grimwood, J.J. McKinnon, M.J. Turner, D. Jayatilaka, M.A. Spackman, *Crystal Explorer 3.1*, University of Western Australia, Perth, Australia, 2012.
- [41] A.D. Becke, *J. Chem. Phys.* 98 (1993) 5648–5652.
- [42] C. Lee, W. Yang, R.G. Parr, *Phys. Rev. B* 37 (1988) 785–789.
- [43] B. Delley, *J. Chem. Phys.* 92 (1990) 508–517.
- [44] A. Tkatchenko, M. Scheffler, *Phys. Rev. Lett.* 102 (2009) 073005.
- [45] R.F.W. Bader, M.T. Carroll, J.R. Cheeseman, C. Chang, *J. Am. Chem. Soc.* 109 (1987) 7968–7979.
- [46] J. Bernstein, R.E. Davis, L. Shimoni, N.-L. Chang, *Angew. Chem. Int. Ed. Engl.* 34 (1995) 1555–1573.
- [47] B. Jerslev, S. Larsen, *Acta Chem. Scand.* 45 (1991) 285–291.
- [48] D.D. Dolliver, B.T. Bhattacharai, A. Pandey, M.L. Lanier, A.S. Bordelon, S. Adhikari, J.A. Dinsler, P.F. Flowers, V.S. Wills, C.L. Schneider, K.H. Shaughnessy, J.N. Moore, S.M. Raders, T.S. Snowden, A.S. McKim, F.R. Fronczek, *J. Org. Chem.* 78 (2013) 3676–3687.
- [49] B.H. Hwang, E.B. Choi, H.K. Lee, H.C. Yang, B.Y. Chung, C.S. Pak, *Synthesis* 2008 (2008) 3569–3578.
- [50] M. Köç, Y. Zorlu, Ü. İsci, S. Berber, V. Ahsen, F. Dumoulin, *CrystEngComm* 18 (2016) 1416–1426.
- [51] M. Kertesz, C.H. Choi, S. Yang, *Chem. Rev.* 105 (2005) 3448–3481.
- [52] U. Salzner, P.G. Pickup, R.A. Poirier, J.B. Lagowski, *J. Phys. Chem. A* 102 (1998) 2572–2578.
- [53] CAMEO chemicals, <https://cameochemicals.noaa.gov/react/75>, 2017 (accessed 10 January 2017).